

Active Disturbance Rejection Controller for Smooth Speed Control of Electric Drives Using Adaptive Generalized Integrator Extended State Observer

Yuefei Zuo ^{ID}, Member, IEEE, Jingwei Zhu ^{ID}, Wenhao Jiang ^{ID}, Shuangchun Xie ^{ID}, Student Member, IEEE, Xiaoyong Zhu ^{ID}, Member, IEEE, Wen-Hua Chen ^{ID}, Fellow, IEEE, and Christopher H. T. Lee ^{ID}, Senior Member, IEEE

Abstract—To suppress the torque ripple for smooth speed control of electric drives, active disturbance rejection (ADR) controller based on generalized integrator (GI) extended state observer (ESO) (GIESO) is developed in this article. Deadbeat ADR controller is employed to control the current, allowing the current control algorithm to be simplified. An adaptive GIESO is developed to address the instability problem caused by the two-step delay in the current control loop. Based on the system stability analysis, the design guideline for the adaptive resonant gain is determined. The proposed adaptive GIESO allows the system to be stable across the entire speed range while suppressing speed ripple to within 1 r/min.

Index Terms—Active disturbance rejection (ADR) control, generalized integrator (GI), resonant control, torque ripple.

I. INTRODUCTION

IN RECENT years, permanent-magnet synchronous motor (PMSM) has attracted lots of attention in direct-drive applications [1] due to its simple structure and high-torque density [2]. However, the large low-order torque ripple due to the open slot and manufacturing imperfection causes speed ripple, resulting in large vibration, acoustic noise, and low control precision [3]. The dominant torque ripple sources include cogging torque, flux harmonics, current harmonics, and current measurement error [4]. To alleviate the effect of torque ripple, there are two types of methods that can be used [5]. The first group of technologies includes motor-design techniques, such as

Manuscript received 22 June 2022; revised 6 October 2022; accepted 28 November 2022. Date of publication 1 December 2022; date of current version 14 February 2023. This work was supported by National Research Foundation (NRF) Singapore under its NRF Fellowship Grant NRF-NRFF12-2020-0003. Recommended for publication by Associate Editor Y. A.-R. I. Mohamed. (Corresponding author: Christopher H. T. Lee.)

Yuefei Zuo, Jingwei Zhu, Shuangchun Xie, and Christopher H. T. Lee are with the School of Electrical, Electronic Engineering, Nanyang Technological University, Singapore 639798 (e-mail: yuefei.zuo@ntu.edu.sg; zhuj0027@e.ntu.edu.sg; shuangch001@e.ntu.edu.sg; CHTLEE@NTU.EDU.SG).

Wenhao Jiang and Xiaoyong Zhu are with the School of Electrical, Information Engineering, Jiangsu University, Zhenjiang 212013, China (e-mail: 2222007090@stmail.ujs.edu.cn; zxyff@ujs.edu.cn).

Wen-Hua Chen is with the Department of Aeronautical, Automotive Engineering, Loughborough University, Loughborough LE11 3TU, UK. (e-mail: w.chen@lboro.ac.uk).

Color versions of one or more figures in this article are available at <https://doi.org/10.1109/TPEL.2022.3226160>.

Digital Object Identifier 10.1109/TPEL.2022.3226160

skewing [6], stator pole arc design [7], and permanent magnet magnetic design [8]. However, these procedures are expensive and only applicable to newly developed machines. Active-control techniques are the second category of methods, which are preferred due to their low costs and flexibility. Among many active control techniques, the speed-control techniques realize a smooth speed control by the torque compensation based on the observed disturbance, are attracting more attentions in many applications [9]. In these speed-control methods, the key technique is the disturbance observation.

Typically, there are two ways to observe the disturbance. One is to use the integrator in the feedback controller. When the reference is a direct signal, zero steady-state error can be secured by using a conventional proportional-integral (PI) controller. When the reference is an alternate signal, however, generalized integrator (GI) or resonant controller should be used [10]. The resonant controller in the stationary reference frame is equivalent to the integrator in the synchronous reference frame [11], which is another efficient technique in suppressing harmonics at the expense of additional frame transformation. When both direct signal and alternate signal exist in the reference, the so-called proportional-integral-resonant (PIR) controller should be employed [12]. In the case of multiple harmonics suppression, either multiple resonant controllers [13], or repetitive controller [14] can be employed.

Although these controllers have a good periodic disturbance rejection performance, they degrade the tracking performance at the same time because they are one-degree-of-freedom controllers. To solve this problem, a two-degree-of-freedom (TDOF) controllers can be employed. In [15], a tracking differentiator is used as a prefilter to smooth the speed reference so that the high-frequency components in the speed reference will not be amplified by the PIR controller. Alternatively, Hu et al. [16] used a partial prefilter, i.e., the prefilter is only used for the resonant controller while a normal PI controller is used for suppressing constant disturbances. Nevertheless, the parameter setting of the partial prefilter is troublesome.

The alternative way to observe the disturbance is to use disturbance observers (DOBs), by which TDOF control can be achieved naturally [17]. The goal of DOBs is to estimate the disturbance by forcing the estimated output to track the real system output. Similarly, regulators used in the feedback control

can be used in observers. For example, proportional regulator in DOB, PI regulator in extended state observer (ESO). It is known from that different DOBs act as a low-pass filter when observing disturbances [18]. Therefore, the generalized PI observers [19] cannot well observe the period disturbances.

In [20], DOB (the alleged dual loop structure) based on resonant regulator is employed to suppress the sixth order current harmonics caused by the deadtime effect. However, the experiments are conducted in the low-speed range and the highest resonant frequency is only 60 Hz. A general design procedure of this kind of DOB and the stability analysis can be found in [21]. Compared with the DOB-based control method, active disturbance rejection (ADR) control (ADRC) based on ESO has a better measurement noise suppression performance because both the speed and disturbance are observed. In [22], generalized integrator ESO (GIESO) is employed to suppress the current harmonics caused by the unbalanced grid. Multiple GI modules are adopted to suppress the fundamental, the second order, and the sixth-order harmonics. So, the highest resonant frequency in the system reaches 300 Hz. However, higher frequency disturbances are not considered and thus the effect of the one-step delay caused by pulselength modulation (PWM) update is not taken into account. In [23], quasi-resonant ESO is developed to improve system's robustness to frequency deviations. The controller is designed in the discrete-time domain so that the one-step delay can be easily handled. The analysis shows that the system will be unstable if the sampling time is two large. Nevertheless, high-frequency disturbances are not considered either. To reject the high-order torque ripple harmonics, Hu et al. [4] employed the PIR controller for current control so that the delay caused by inner current loop can be eliminated. However, the PIR current controller complicates the algorithm.

In this article, active disturbance rejection (ADR) controller using GIESO is used to achieve smooth speed control of electric drives. Different from the system in [4], the system in this article adopts the widely used deadbeat active disturbance rejection controller [24] for current control. To solve the instability problem caused by the two-step delay in the current control loop, an adaptive GIESO is developed. In such a case, the complicated PIR controller can be avoided. To obtain the design guideline for the adaptive resonant gain, the critical resonant frequency for stable operation is deduced. Various experiments are tested on the dSPACE DS1103 test bench to verify the effectiveness of the proposed method.

The rest of this article is organized as follows. In Section II, ADR controller based on GIESO is designed, followed by the system performance analysis in Section III. In Section IV, the design guideline for the adaptive resonant gain is presented. Experimental results are presented and analyzed in Section V. Finally, Section VI concludes this article.

II. ADR CONTROLLER BASED ON GIESO

A. Mathematical Model of Mechanical System

The motion equation of the PMSM system with known moment of inertia can be given as

$$\dot{\Omega} = (-B\Omega + T_e - T_L)/J = bT_e + d_n = bT_e^* + d_{to} \quad (1)$$

where Ω , B , J , and T_L denote the mechanical angular velocity, the moment of inertia, the viscous friction torque coefficient, and the load torque, respectively; $b = 1/J$ is the control gain, T_e and T_e^* represent the electromagnetic torque and its reference value; the viscous friction torque coefficient is very small and is usually assumed to be zero, so the viscous friction torque and the load torque are lumped as the nominal disturbance $d_n = -(B\Omega + T_L)/J$; $d_{to} = d_n - b(T_e^* - T_e)$ is the total disturbance considering the torque tracking error.

In many applications, conventional ESO-based ADR controller is employed to reject a constant disturbance d_{con} . However, when both a constant disturbance d_{con} and a sinusoidal disturbance d_{sin} with a frequency of ω_h exists in the system, the mathematical model should be modified as

$$\begin{cases} \dot{\Omega} = bT_e^* + d_{con} + d_{sin} \\ \dot{d}_{con} = 0 \\ \dot{d}_{sin} = d_{cos} \\ \dot{d}_{cos} = -\omega_h^2 d_{sin} \end{cases} \quad (2)$$

where d_{cos} is the derivative of d_{sin} .

B. Feedback Control Law

Defining the reference of mechanical angular velocity as Ω^* , then the tracking error of mechanical angular velocity can be expressed as $e_s = \Omega^* - \Omega$ and we have

$$\dot{e}_s = \dot{\Omega}^* - \dot{\Omega} = \dot{\Omega}^* - bT_e^* - d_{to}. \quad (3)$$

The expected error convergence law can be designed as

$$\dot{e}_s = -k_{ps}e_s \quad (4)$$

where k_{ps} is the proportional gain.

Substituting (4) into (3) yields

$$T_e^* = \frac{\dot{\Omega}^* + k_{ps}(\Omega^* - \Omega) - d_{to}}{b}. \quad (5)$$

In (5), the disturbance d_{to} is unknown. Generally, the rotor position is obtained from the position sensors such as the encoder or resolver, and the speed Ω can be calculated by the derivative of the mechanical angular position θ_m . Due to the quantization error in the measurement of the position, the speed calculated by the classical frequency method is contaminated by the measurement noise [25], [26]. Denoting the measurement noise in position and speed as δ_p and δ_n , $\delta_n(s) = s\delta_p(s)$, then the measured speed can be expressed as $\Omega^m = \Omega + \delta_n$. When Ω and d_{to} are substituted by their estimated value $\hat{\Omega}$ and \hat{d}_{to} , the torque reference is modified as

$$T_e^* = \frac{\dot{\Omega}^* + k_{ps}(\Omega^* - \hat{\Omega}) - \hat{d}_{to}}{b}. \quad (6)$$

In the practical system, the reference torque limit is usually applied as follows:

$$T_{esat}^* = \begin{cases} T_{e\max}^* \text{sign}(T_e^*), & |T_e^*| > T_{e\max}^* \\ T_e^*, & |T_e^*| \leq T_{e\max}^* \end{cases} \quad (7)$$

where T_{esat}^* and $T_{e\max}^*$ are the saturated torque reference and the maximum torque reference, respectively.

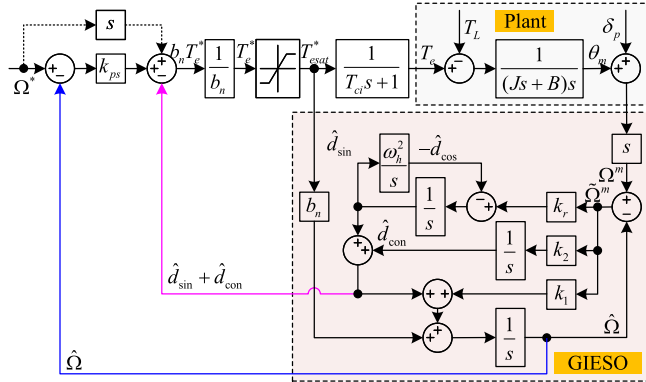


Fig. 1. Block diagram of the modified ADRC system.

According to (1), the relationship between the torque reference and the total disturbance can be expressed by

$$bT_e^*(s) = s\Omega(s) - d_{\text{to}}(s) = s\Omega^m(s) - [d_{\text{to}}(s) + s\delta_n(s)]. \quad (8)$$

Without considering the saturation of torque reference, the measured speed can be obtained by substituting (8) into (6)

$$\Omega^m(s) = \Omega^*(s) + \frac{k_{\text{ps}}}{s + k_{\text{ps}}} \tilde{\Omega}^m(s) + \frac{1}{s + k_{\text{ps}}} [\tilde{d}_{\text{to}}(s) + s\delta_n(s)] \quad (9)$$

where $\tilde{\Omega}^m = \Omega^m - \hat{\Omega}$ and $\tilde{d}_{\text{to}} = d_{\text{to}} - \hat{d}_{\text{to}}$ are the speed observation error and the disturbance observation error.

From (9), it can be seen that the control performance depends not only on the feedback control law but also on the speed observation error and the disturbance observation error.

C. Speed and Disturbance Observation Using GIESO

Considering the sinusoidal disturbance, a GIESO is constructed as

$$\begin{cases} \dot{\tilde{\Omega}}^m = \Omega^m - \hat{\Omega} = \Omega + \delta_n - \hat{\Omega} \\ \dot{\hat{\Omega}} = bT_e^* + \hat{d}_{\text{con}} + \hat{d}_{\text{sin}} + k_1 \tilde{\Omega}^m \\ \dot{\hat{d}}_{\text{con}} = k_2 \tilde{\Omega}^m \\ \dot{\hat{d}}_{\text{sin}} = \hat{d}_{\text{cos}} + k_r \tilde{\Omega}^m \\ \dot{\hat{d}}_{\text{cos}} = -\omega_h^2 \hat{d}_{\text{sin}} \end{cases} \quad (10)$$

where variables with $\hat{\cdot}$ represents the estimated value, k_r is the resonance gain of the GI.

In this article, the ADR controllers based on the conventional ESO and the GIESO are called the conventional ADR controller and the modified ADR controller, the control systems using these two controllers are noted as the conventional ADRC system and the modified ADRC system, respectively. The block diagram of the modified ADRC system is shown in Fig. 1. When $k_r = 0$, the modified ADRC system is the same as the conventional ADRC system.

From Fig. 1, the speed observation error, the estimated speed and disturbance can be deduced as

$$\begin{cases} \tilde{\Omega}^m(s) = \frac{s}{G_0(s)} [s\Omega^m(s) - bT_e^*(s)] \\ \hat{\Omega}(s) = \Omega^m(s) - \tilde{\Omega}^m(s) \\ \hat{d}_{\text{to}}(s) = \left[1 - \frac{\Delta_2 - k_2}{G_0(s)}\right] \tilde{\Omega}^m(s) \end{cases} \quad (11)$$

where $G_0(s) = \Delta_2 + k_r s G_{\text{GI}}(s) = s^2 + k_1 s + k_2 + k_r \frac{s^2}{s^2 + \omega_h^2}$, $\Delta_2 = s^2 + k_1 s + k_2$ is the characteristic polynomial of the conventional ESO, and $G_{\text{GI}}(s) = \frac{s}{s^2 + \omega_h^2}$ is the transfer function of the GI.

Generally, Δ_2 is set as $(s + \omega_o)^2$, thus, k_1 and k_2 can be calculated by $k_1 = 2\omega_o$ and $k_2 = \omega_o^2$, ω_o is the natural frequency of the conventional ESO.

D. System Output Considering the Torque Control Loop

Substituting (11) into (6) yields

$$bT_e^*(s) = \frac{G_0(s)(s + k_{\text{ps}})}{G_3(s)} [\Omega^*(s) - \Omega^m(s)] + s\Omega^m(s) \quad (12)$$

where $G_3(s) = k_{\text{ps}}s + \Delta_2 - k_2 = s(s + k_{\text{ps}} + k_1)$.

Suppose the torque control system can be modeled as a first-order low-pass filter with a time constant of T_{ci} . The relationship between the torque reference and the total disturbance can be expressed by

$$bT_e^*(s) = (T_{\text{ci}}s + 1) \{s\Omega^m(s) - [d_n(s) + s\delta_n(s)]\}. \quad (13)$$

Substituting (13) into (11) yields

$$\begin{cases} \tilde{\Omega}^m(s) = \frac{s}{G_0(s)} D(s) \\ \hat{d}_{\text{to}}(s) = \left[1 - \frac{\Delta_2 - k_2}{G_0(s)}\right] D(s) \\ D(s) = (T_{\text{ci}}s + 1) [d_n(s) + s\delta_n(s)] - T_{\text{ci}}s^2 \Omega^m(s). \end{cases} \quad (14)$$

Substituting (13) into (12) yields

$$\begin{aligned} \Omega^m(s) &= \frac{(s + k_{\text{ps}}) G_0(s)}{\Delta_{\text{cl}}} \Omega^*(s) \\ &\quad + \frac{(T_{\text{ci}}s + 1) G_3(s)}{\Delta_{\text{cl}}} [d_n(s) + s\delta_n(s)] \end{aligned} \quad (15)$$

where $\Delta_{\text{cl}} = T_{\text{ci}}s^2 G_3(s) + (s + k_{\text{ps}}) G_0(s)$ is the characteristic polynomial of the closed-loop control system.

III. SYSTEM DYNAMIC PERFORMANCE AND STABILITY

A. System Dynamic Performance

When $T_{\text{ci}} = 0$, from (14) and (15), it is known that the transfer functions from the actual disturbance to the observed disturbance, from the disturbance to the output, and from the measurement noise to the output can be expressed as

$$\begin{cases} \Phi_d^{\text{GIESO}}(s) = \frac{\hat{d}_{\text{to}}(s)}{d_{\text{to}}(s)} = \frac{k_2 + k_r s G_{\text{GI}}(s)}{G_0(s)} \\ \Phi_d(s) = \frac{\Omega(s)}{d_{\text{to}}(s)} = \frac{G_3(s)}{G_0(s)(s + k_{\text{ps}})} \\ \Phi_n(s) = \frac{\Omega(s)}{-\delta_n(s)} = 1 - s\Phi_d(s). \end{cases} \quad (16)$$

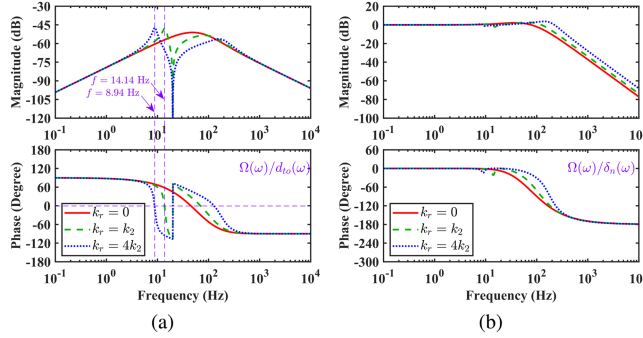


Fig. 2. Dynamic performance of the modified ADRC system under different λ when ω_h is 20 Hz. (a) Disturbance rejection property. (b) Measurement noise suppression performance.

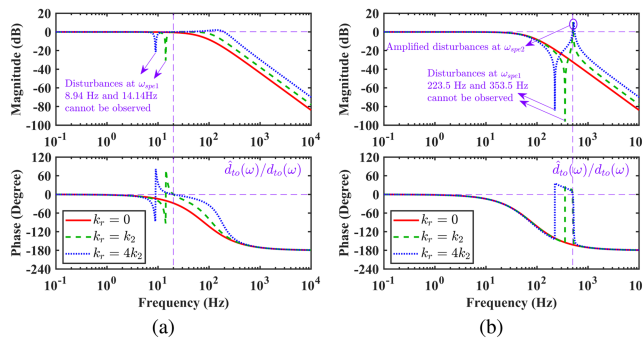


Fig. 3. Disturbance observation property of GIESO under different λ when ω_h is 20 Hz and 500 Hz.

It shows that the disturbance rejection ability and the measurement noise suppression performance are decided by k_{ps} and the transfer function $G_0(s)$, $G_3(s)$.

Setting $k_{ps} = 300$ rad/s and $\omega_o = 500$ rad/s, when ω_h is set as 20 Hz, dynamic performances of the modified ADRC system and the conventional ADRC system are shown in Fig. 2. From Fig. 2(a), it can be seen that the disturbance of the 20 Hz resonant frequency can be well suppressed by the modified ADRC system, but cannot be suppressed by the conventional ADRC system. Using larger k_r can reject a wider range of disturbances and reduce the sensitivity to the resonant frequency, but it also leads to poor measurement noise suppression performance, as shown in Fig. 2(b).

From Fig. 2(a), it is also observed that the modified ADRC system has poorer rejection property for disturbances near 8.94 Hz and 14.14 Hz than the conventional ADRC system, this is because the GIESO cannot observe the disturbance of a specific frequency that lower than the resonant frequency, as shown in Fig. 3(a). According to the first equation in (16), the specific frequency ω_{spe1} can be deduced as

$$\omega_{spe1} = \frac{\omega_h}{\sqrt{1 + \lambda}} \quad (17)$$

When λ is 1 and 4, the specific frequency is $0.707\omega_h$ and $0.447\omega_h$, respectively, this explains why the frequency is 8.94 Hz and 14.14 Hz when ω_h is 20 Hz. The conclusion is also true when $\omega_h = 500$ Hz, as proved by Fig. 3(b). Since the disturbance

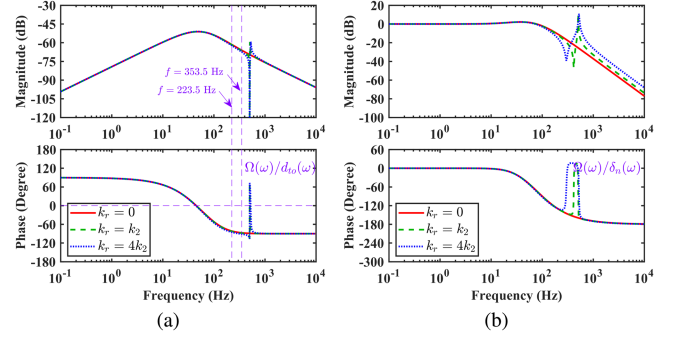


Fig. 4. Dynamic performance of the modified ADRC system under different λ when ω_h is 500 Hz. (a) Disturbance rejection property. (b) Measurement noise suppression performance.

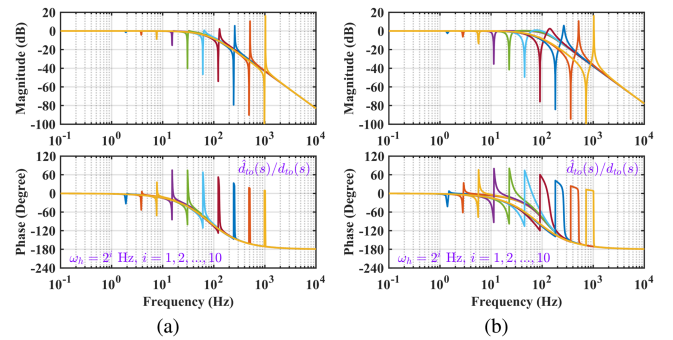


Fig. 5. Disturbance observation property of the GIESO under different λ . (a) $\lambda = 0.1$. (b) $\lambda = 1.0$.

with the frequency of ω_{spe1} cannot be observed by GIESO, it is suppressed by the proportional feedback control. It should be pointed out that in the conventional ADRC system, the disturbance in the low-frequency range is mainly rejected by the disturbance feedforward control, while the disturbance in the high-frequency range is mainly suppressed by the feedback control [19]. Therefore, the modified ADRC system is inferior to conventional ADRC system in rejecting the specific frequency disturbance in the low-frequency range, but its suppression performance of the specific frequency disturbance in the high-frequency range is almost the same as that of the conventional ADRC system, as shown in Fig. 2(a) and 4(a).

From Fig. 3(b), it can also be found that the disturbance of another specific frequency ω_{spe2} that higher than the resonant frequency is obviously amplified by GIESO in the high-frequency range. This property has little effect on the disturbance rejection ability, but it has large effect on the measurement noise suppression performance, as shown in Fig. 4(b). To have a better understanding of this phenomenon, bode plots under different ω_h are shown in the same figure. With the same k_{ps} and ω_o , when λ is 0.1 and 1.0, bode plots of the disturbance observation property of the GIESO under different ω_h are shown in Fig. 5, bode plots of the disturbance rejection property and the measurement noise suppression performance of the modified ADRC system under different ω_h are shown in Figs. 6 and 7. It can be seen that the use of GI leads to a decrease in the rejection property for disturbances with frequencies around ω_{spe1} and a

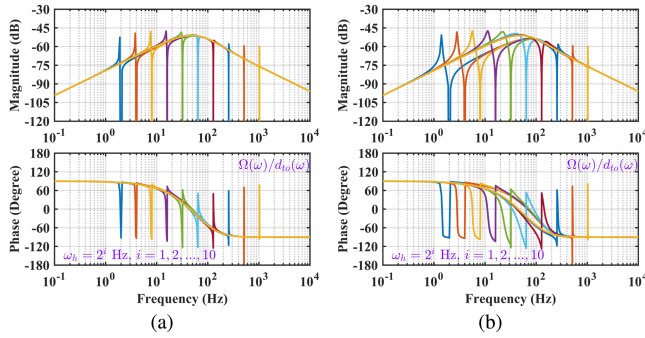


Fig. 6. Disturbance rejection property of the modified ADRC system under different λ . (a) $\lambda = 0.1$. (b) $\lambda = 1.0$.

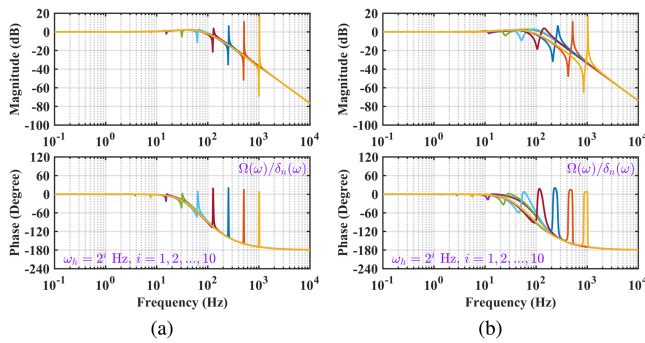


Fig. 7. Noise suppression performance of the modified ADRC system under different λ . (a) $\lambda = 0.1$. (b) $\lambda = 1.0$.

decrease in the measurement noise suppression performance for noises with frequencies around ω_{spe2} . Using smaller λ mitigates the performance degradation, but increases the sensitivity to the resonant frequency. In the experiments, λ should be carefully tuned to achieve the desired performance.

B. System Stability of the Conventional ADRC System

When $k_r = 0$, the modified ADRC system is the same as the conventional ADRC system and there is $G_0(s) = \Delta_2$. The characteristic polynomial of the conventional ADRC system can be deduced as

$$\Delta_{cl} = (s + k_{ps})(s^2 + k_1 s + k_2) + T_{ci} s^3 (s + k_{ps} + k_1). \quad (18)$$

To evaluate the effect of T_{ci} , root locus when T_{ci} varies can be plotted. The open-loop transfer function in a unit negative feedback control system with the same characteristic polynomial can be expressed as

$$G_{T_{ci}}(s) = T_{ci} \frac{s^3 (s + k_{ps} + k_1)}{(s + k_{ps})(s^2 + k_1 s + k_2)}. \quad (19)$$

Setting $k_{ps} = 300$ rad/s, the plots of root locus with the variation of T_{ci} when ω_o is 500 rad/s and 1000 rad/s are shown in Fig. 8. It can be seen that the condition for stable operation is $T_{ci} < 4.52$ ms and $T_{ci} < 3.47$ ms when ω_o is 500 and 1000 rad/s, respectively.

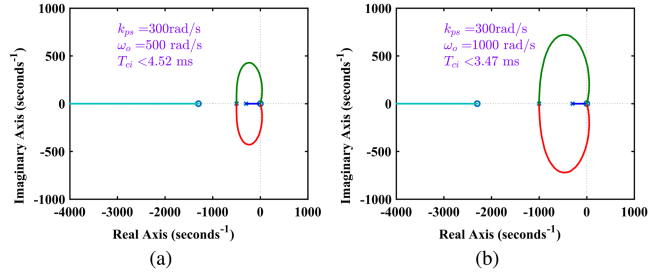


Fig. 8. Root locus when T_{ci} varies under different ω_o . (a) $\omega_o = 500$ rad/s. (b) $\omega_o = 1000$ rad/s.

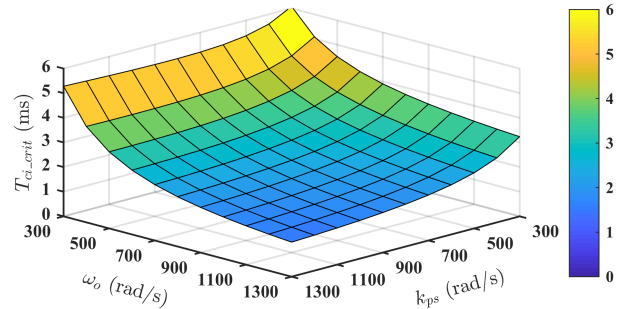


Fig. 9. T_{ci_crit} under different k_{ps} and ω_o .

According to the Routh–Hurwitz stability criterion, the critical value of T_{ci} for stable operation T_{ci_crit} under different k_{ps} and ω_o can be calculated and the plot is shown in Fig. 9. It can be seen that T_{ci_crit} decreases as k_{ps} or ω_o increases. From (18), it is easy to know that the system is stable when $T_{ci} = 0$. As a result, it is learned that the delay in torque control loop makes the conventional ADRC system unstable.

To improve the system stability, torque control method with high bandwidth should be adopted. For example, PIR controller is employed for current regulation in [4]. However, the measures to deal with the deteriorated tracking performance caused by the PIR controller complicates the algorithm [16].

In this article, deadbeat current vector control is employed to control the torque. By using the deadbeat control, the actual torque lags the reference torque with two control steps when the voltage is not saturated [27], the minimum value of the time constant of the torque control loop is twice the sampling time, i.e., $2T_s$ [24]. In this article, the sampling time is set as 0.1 ms, so the minimum value of T_{ci} is 0.2 ms.

C. System Stability of the Modified ADRC System

The characteristic polynomial of the modified ADRC system can be obtained as

$$\Delta_{cl} = (s + k_{ps}) \left[(s^2 + k_1 s + k_2) + k_r \frac{s^2}{s^2 + \omega_h^2} \right] + T_{ci} s^3 (s + k_{ps} + k_1). \quad (20)$$

Traditionally, the delay caused by the torque control loop is not considered, i.e., $T_{ci} = 0$. In this case, the characteristic

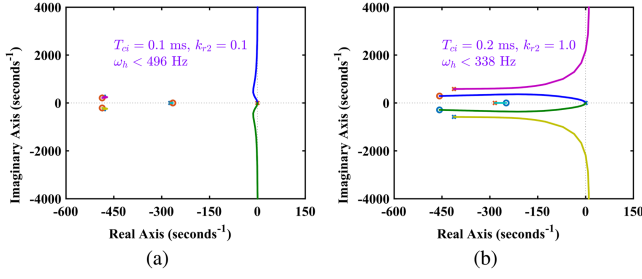


Fig. 10. Root locus when ω_h varies under different T_{ci} and λ . (a) $T_{ci} = 0.1 \text{ ms}$, $\lambda = 0.1$. (b) $T_{ci} = 0.2 \text{ ms}$, $\lambda = 1.0$.

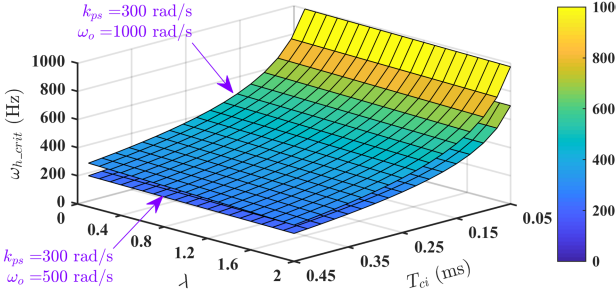


Fig. 11. ω_{h_crit} varies with T_{ci} and λ .

polynomial of the closed-loop control system is simplified as

$$\Delta_{cl} = (s + k_{ps}) \left[(s^2 + k_1 s + k_2) + k_r \frac{s^2}{s^2 + \omega_h^2} \right]. \quad (21)$$

According to the Routh–Hurwitz stability criterion, the system is always stable regardless of the value of k_r .

When $T_{ci} \neq 0$, it is known from (20) that the system stability varies with the resonant frequency ω_h . To evaluate the effect of ω_h , root locus when ω_h varies can be plotted. The open-loop transfer function in a unit negative feedback control system with the same characteristic polynomial can be expressed as

$$G_{\omega_h}(s) = \omega_h^2 \frac{(s + k_{ps}) \Delta_2 + T_{ci} s^2 G_3(s)}{[T_{ci} s^2 G_3(s) + (s + k_{ps})(\Delta_2 + k_r)] s^2}. \quad (22)$$

Defining the ratio k_r to k_2 as $\lambda = k_r/k_2$. When $k_{ps} = 300 \text{ rad/s}$ and $\omega_o = 500 \text{ rad/s}$, the plots of root locus when ω_h varies under different T_{ci} and λ are shown in Fig. 10. It can be seen from Fig. 10(b) that ω_{h_crit} is 338 Hz when $T_{ci} = 0.2 \text{ ms}$, $\lambda = 1.0$. If GI is used to suppress the 12th harmonic, then the speed limit for stable operation is 1690 r/min. However, if GI is used to suppress the 60th harmonic, then the speed limit for stable operation is only 338 r/min.

According to the Routh–Hurwitz stability criterion, the critical ω_h for stable operation ω_{h_crit} can be calculated. When $k_{ps} = 300 \text{ rad/s}$, ω_o is 500 rad/s, and 1000 rad/s, ω_{h_crit} under different λ and T_{ci} is shown in Fig. 11. It shows that ω_{h_crit} can be increased by either decreasing λ or decreasing T_{ci} , with the latter having a greater effect.

When $T_{ci} = 0.2 \text{ ms}$ and $\lambda = 1$, the plots of root locus when ω_h varies under different k_{ps} and ω_o are shown in Fig. 12. Compared with Fig. 10(b), it can be concluded that increasing k_{ps} from 300

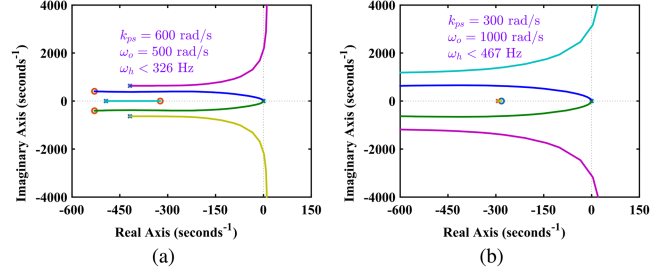


Fig. 12. Root locus when ω_h varies under different k_{ps} and ω_o . (a) $k_{ps} = 600 \text{ rad/s}$, $\omega_o = 500 \text{ rad/s}$. (b) $k_{ps} = 300 \text{ rad/s}$, $\omega_o = 1000 \text{ rad/s}$.

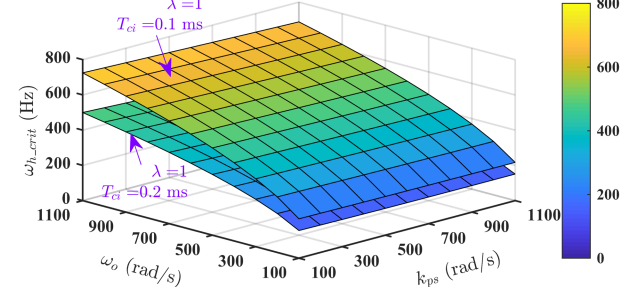


Fig. 13. ω_{h_crit} varies with k_{ps} and ω_o .

to 600 rad/s decreases ω_{h_crit} from 338 to 326 Hz, but increasing ω_o from 500 to 1000 rad/s increases it from 338 to 467 Hz.

When $\lambda = 1$, T_{ci} is 0.1 ms and 0.2 ms, the plot of ω_{h_crit} varies with k_{ps} and ω_o is shown in Fig. 13. It indicates that increasing ω_{h_crit} can be accomplished by either decreasing k_{ps} or increasing ω_o . It should be pointed out that decreasing k_{ps} has little effect on increasing ω_{h_crit} .

In summary, the modified ADRC system will be unstable as the resonant frequency increases due to the limited bandwidth of ESO and the delay caused by the torque control loop. Although the frequency limit can be increased by decreasing T_{ci} or increasing ω_o , large ω_o results in poor measurement noise suppression performance, whereas small T_{ci} has a high requirement for hardware. To this end, adaptive GIESO is developed in this article.

IV. ADAPTIVE GIESO

Since high-frequency torque ripple has little effect on the speed but leads the system to be unstable, the high-order harmonics suppression can be removed in the high-speed range. As a result, an adaptive GIESO with variable resonance gain is proposed in this article. The gain of the GI for the suppression of 60th harmonic is decreased as speed increases so that the GI only acts in the low-frequency range. The adaptive resonance gain is expressed by

$$k_{r1} = \lambda k_2 (1 - k\omega_r) = k_r (1 - kp_n \pi n / 30) \quad (23)$$

where k is a positive gain, p_n is the polePairs.

According to the motion equation, the speed ripple caused by the torque ripple depends on the amplitude of torque ripple as well as the system inertia. Under the same torque ripple, the

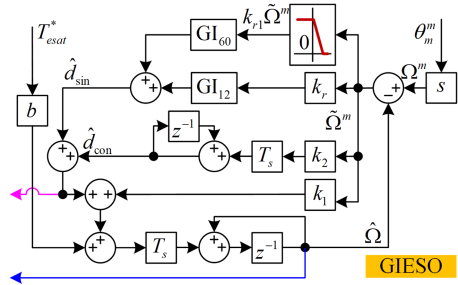


Fig. 14. Block diagram of the proposed adaptive GIESO.

TABLE I
SPECIFICATION OF THE PMSM

Symbol	Quantity	Symbol	Quantity
Rated power P_N	1.0 (kW)	polePair numbers p_n	10
Rated voltage U_N	100 (V)	D -axis inductance L_d	6.7 (mH)
Rated speed n_N	600 (r/min)	Q -axis inductance L_q	6.7 (mH)
Rated torque T_N	16 (N·m)	Permanent flux ψ_f	0.122 (Wb)
Current limit $I_s \text{ max}$	9.0 (A)	Torque constant K_t	1.83 (N·m/A)
Stator resistance R_s	0.7 (Ohm)	Motor system inertia J	2.67 (g · m ²)

speed ripple in the system with larger inertia will be smaller. Therefore, the adaptive gain should be designed according to the actual system.

From Fig. 10(b), it is known that the speed limit is 338 r/min when $k_{ps} = 300$ rad/s, $\omega_o = 500$ rad/s, and $T_{ci} = 0.2$ ms. In addition, in the experiments, we found that the 60th speed ripple at the speed over 200 r/min is smaller than 1.5 r/min. Therefore, to make the system stable in the whole speed range, the gain k can be set by making k_{r1} equals 0 at the speed ranges from 200 to 338 r/min. Consequently, k should be set between 0.0028 and 0.0048. In this article, the two k for the module is set as 0.0025 in the system so that k_{r1} equals 0 at the speed of 238.7 r/min. The saturation function can be used to keep k_{r1} nonnegative. The block diagram of the adaptive GIESO is shown in Fig. 14.

V. EXPERIMENTAL VERIFICATION

A. System Configuration

The PMSM studied in this article has 10 pole pairs and 12 slots [28]. The motor specifications are shown in Table I. The configuration of the test bench is shown in Fig. 15. A programmable dc power supply is used to provide 150 V dc-bus voltage. The PMSM is driven by a self-made inverter, consisting of Mitsubishi intelligent power module, current and voltage hall sensors, etc. The dSPACE DS1103-based field-oriented control box is employed for driving the PMSM. The control strategy is based on space vector PWM control with $i_d^* = 0$. Deadbeat current controllers are employed in the current-loop to control i_d and i_q , respectively, and different ADRC controllers are employed in the speed-loop. The current limit is set as 9 A. The sampling frequency, current control frequency, and the speed control frequency are all set to 10 kHz.

The torque ripple of the tested motor is estimated by GIESO, which is employed to suppress the speed ripple. When the speed

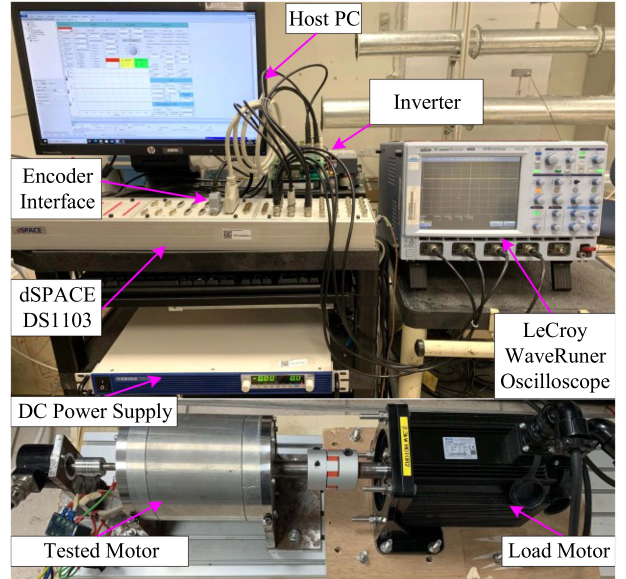


Fig. 15. Configuration of the test bench.

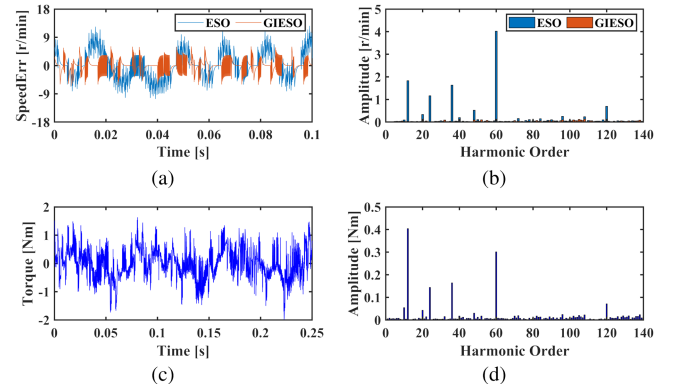


Fig. 16. Tested speed ripple and torque ripple at the speed of 60 r/min. (a) Speed ripple. (b) Spectrum analysis of the speed ripple. (c) Tested torque ripple when using GIESO. (d) Spectrum analysis of the torque ripple.

TABLE II
COMPARISON OF THE SPEED RIPPLE

Speed ripple (r/min)	12 th	24 th	36 th	48 th	60 th	120 th
ESO	1.832	1.165	1.632	0.525	4.019	0.699
GIESO	0.032	0.015	0.016	0.091	0.018	0

ripple is fully suppressed, the estimated disturbance torque is taken as the torque ripple. When $k_{ps} = 300$ rad/s and $\omega_o = 500$ rad/s, the speed ripple when using ESO and GIESO at the speed of 60 r/min is shown in Fig. 16(a), and the spectrum analysis is shown in Fig. 16(b). The comparison of the speed ripple in different ADRC systems are shown in Table II. It can be seen that all the speed ripple harmonics in the GIESO-ADRC system are greatly suppressed. In such case, the estimated torque ripple and its spectrum analysis are shown in Fig. 16(c) and (d), respectively. From Fig. 16(d), it is known that there are

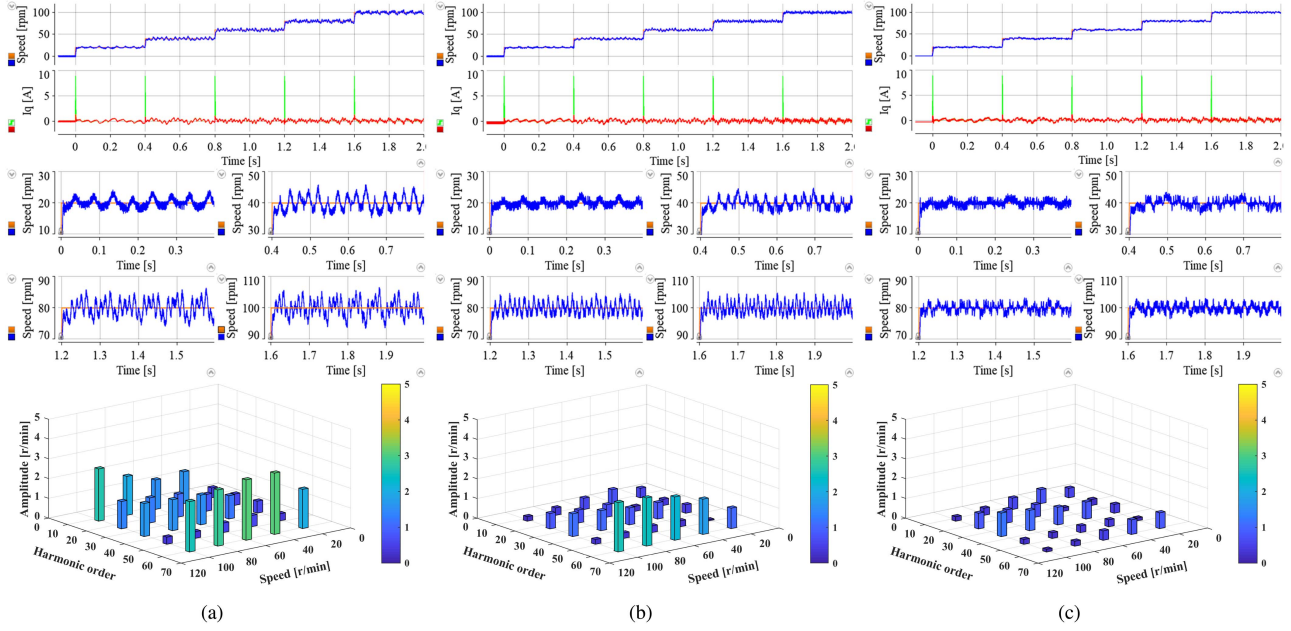


Fig. 17. Speed ripple in the low-speed range. (a) Conventional ADRC. (b) Modified ADRC with 12th harmonic suppression. (c) Modified ADRC with 12th and 60th harmonics suppression.

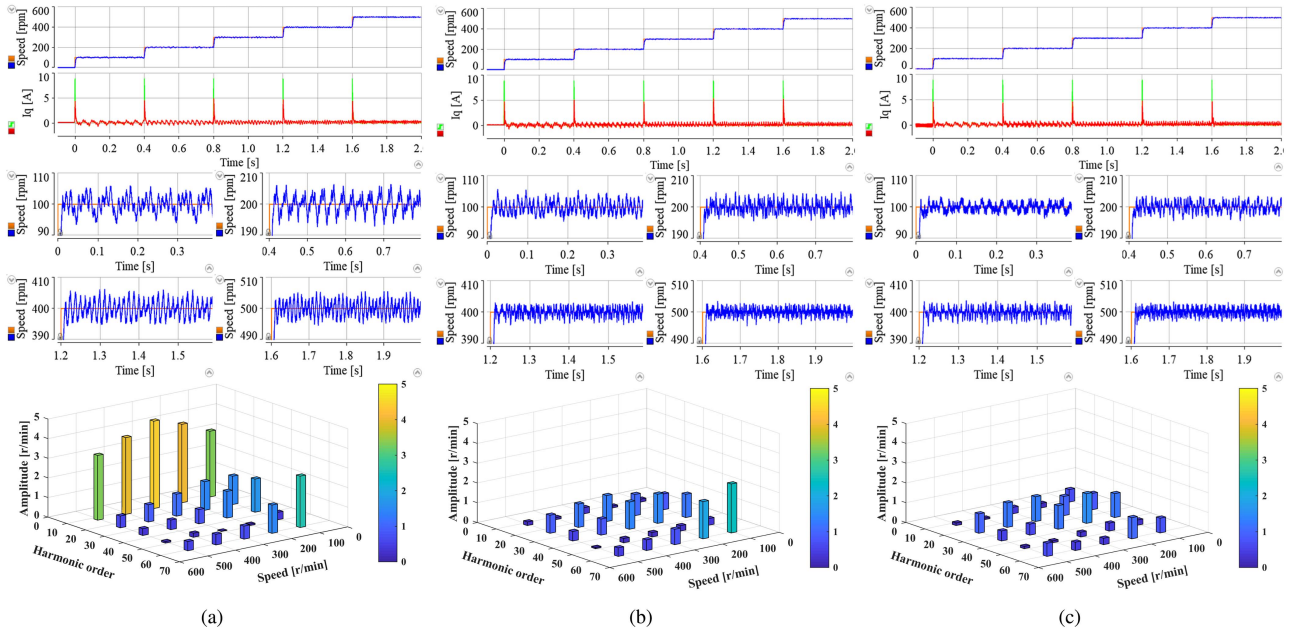


Fig. 18. Speed ripple in the high-speed range. (a) Conventional ADRC. (b) Modified ADRC with 12th harmonic suppression. (c) Modified ADRC with 12th and 60th harmonics suppression.

abundant harmonics in the torque ripple, such as 12th harmonic, 24th harmonic, 36th harmonic, 60th harmonic, and 120th harmonic. According to the analysis results in [3], these low-order harmonics are caused by manufacturing uncertainties, specifically, the imperfection of stator. The frequencies of different order harmonics are speed dependent, i.e., $\omega_h = k_h \omega_r$, k_h is the harmonic order, ω_r is the rotor angular speed. Among these harmonics, the 12th harmonic with the amplitude of 0.4 N·m and the 60th harmonic with the amplitude of 0.3 N·m

are the dominant harmonics. Consequently, only these two harmonics are suppressed in experiments.

B. Performance When Using the Conventional ADR Controller

Since the cogging torque contains different harmonics, the effect of torque ripple on speed feedback will be different under different speed references. Therefore, the speed references in the experiments are stepped from 0 r/min to

100 r/min and 500 r/min in a step of 20 r/min and 100 r/min, respectively.

The speed response of the conventional ADRC system is shown in Figs. 17(a) and 18(a), where the fast Fourier transform (FFT) is implemented on the speed tracking error in the steady state. It can be seen that the speed ripple decreases with the increase of the cogging torque frequency. The 12th order harmonic of the cogging torque causes the largest effect on the speed ripple when the speed is higher than 100 r/min. When the reference speed is 100 r/min, the frequency of the 12th order harmonic is 20 Hz. As shown in Fig. 2(a), the conventional ADRC system has the worst rejection ability for the disturbances at frequencies around 50 Hz, which explains why the 12th speed ripple at the speed of 300 r/min is the largest while the 60th speed ripple at the speed of 40 r/min and 60 r/min are the largest. It is noted that the 60th speed ripple is negligible when the speed is over 200 r/min.

Since the 60th speed ripple is dominant in the low-speed range while the 12th speed ripple is dominant in the high-speed range, only two GI modules are employed in the system, as shown in Fig. 14. The two resonance gain ratio λ for the module GI_{12} and GI_{60} are set as 1.0 and 0.1, respectively.

C. Performance When Using the Modified ADR Controller

When only 12th harmonic suppression is enabled, the speed response of the modified ADRC system is shown in Figs. 17(b) and 18(b). It can be seen that the 12th harmonics are greatly reduced in the whole speed range. Although only the module GI_{12} is employed, the high-order harmonics in the low-speed range ($n < 80$ r/min) is also decreased, which can also be explained by the bode plots shown in Fig. 2(a). Without the 12th speed ripple, the 60th speed ripple becomes the dominant harmonic component.

When both 12th and 60th harmonic suppression is enabled and an adaptive gain k_{r1} is utilized, the speed response of the modified ADRC system is shown in Figs. 17(c) and 18(c). It can be found that both the 12th and the 60th speed ripple are also greatly reduced, which verifies the effectiveness of the proposed method.

Fig. 19 shows the step responses of the modified ADRC system under different combinations of k and λ . It can be seen that the system becomes unstable in the high-speed range when using a constant resonance gain k_{r1} . It should be pointed out that the waveform is captured by using a trigger signal, which acts at the time of 0 s. This explains why there are waveforms before 0 s. In Fig. 19(a), it seems that the system can be stable at the speed of 500 r/min. This is because the system takes longer time to reach the unstable state when using a smaller λ . When λ is increased from 0.1 to 1.0, the experimental results are shown in Fig. 19(c). It is noted that the system becomes unstable at the speed of 300 r/min, which is consistent to the theoretical results. As a comparison, when using the proposed adaptive resonance gain, the system can be stable in the whole speed range, as shown in Fig. 19(b) and (d).

To show the effectiveness of the modified ADRC system in the whole speed range, the tracking performance for two kinds of

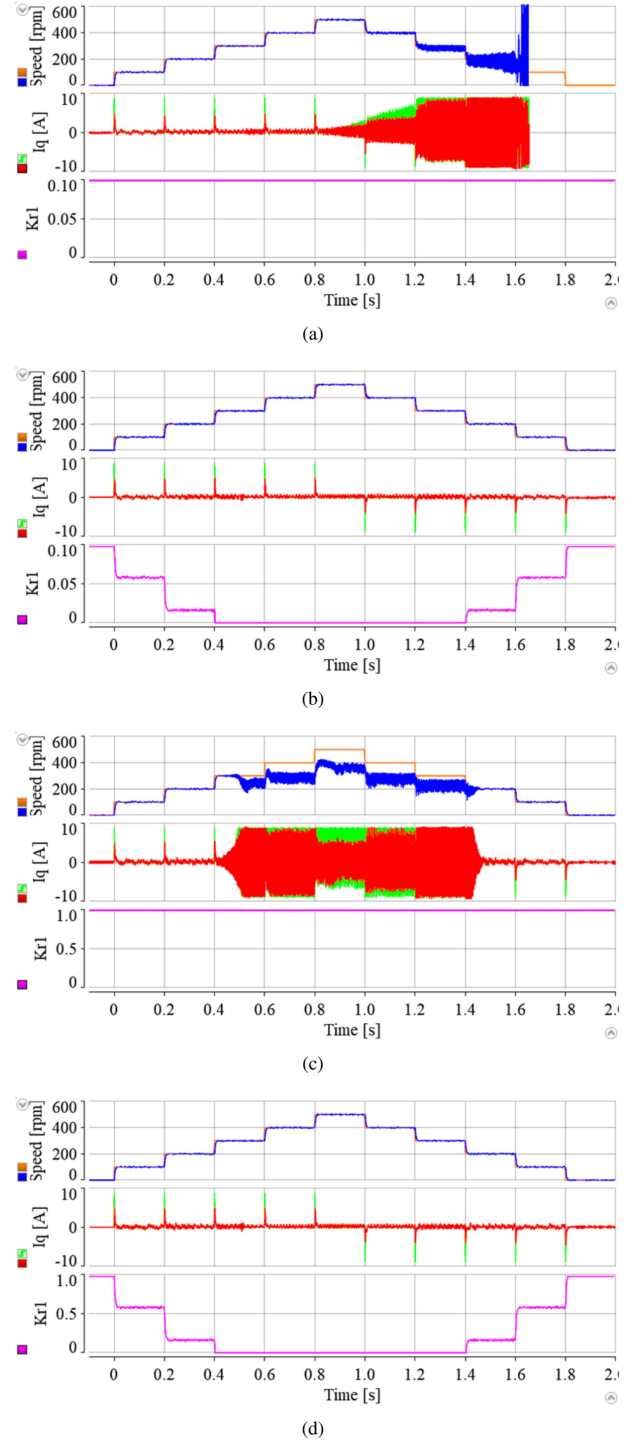


Fig. 19. Transient response of the modified ADRC when tracking step speed references using constant k_{r1} and variable k_{r1} . (a) $\lambda = 0.1, k = 0$. (b) $\lambda = 0.1, k = 0.004$. (c) $\lambda = 1.0, k = 0$. (d) $\lambda = 1.0, k = 0.004$.

sinusoidal speed references expressed by $300 + 300 \sin 4\pi t$ and $600 \sin 4\pi t$ are tested, the speed responses are shown in Fig. 20. It can be seen that when using the conventional ADRC controller, the speed tracking error when tracking the single direction speed and the double direction speed is ± 0.4 rad/s and ± 0.5 rad/s, while they can be reduced by 50% to ± 0.2 rad/s and ± 0.25 rad/s when using the modified ADRC controller.

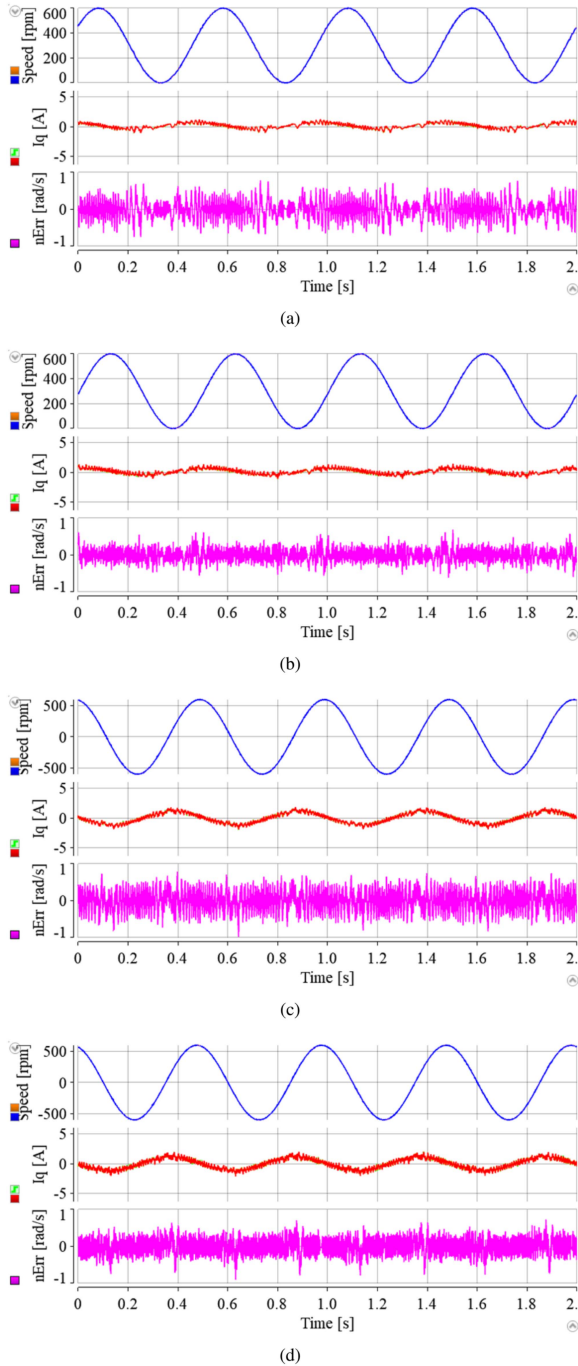


Fig. 20. Comparison of the conventional ADRC and the modified ADRC when tracking sinusoidal speed references. (a) Conventional ADRC, $n = 300 + 300 \sin 4\pi t$. (b) Modified ADRC, $n = 300 + 300 \sin 4\pi t$. (c) Conventional ADRC, $n = 600 \sin 4\pi t$. (d) Modified ADRC, $n = 600 \sin 4\pi t$.

VI. CONCLUSION

In this article, ADR controller based on adaptive GIESO is developed to suppress the torque ripple for smooth speed control of electric drives in the whole speed range. The GIESO with fixed resonance gain is effective for the low-order harmonics in the whole speed range, while it leads the system to be unstable in

the high-speed range when rejecting high-order harmonics. The reason behind this is the limited bandwidth of the torque control loop and the limited bandwidth of ESO. High bandwidth of the torque control loop can be realized by using deadbeat control, while the increase of ESO bandwidth is restricted by the speed measurement noise. To make a stable operation in the whole speed range, an adaptive resonance gain can be adopted. By using the proposed adaptive GIESO, both the 12th and the 60th speed ripple can be suppressed within 1 r/min in the whole speed range when tracking constant speed references. Compared with the conventional ADR controller, the proposed ADR controller can reduce the speed tracking error by 50% when tracking the sinusoidal speed references. Since delay also exists in the PWM undate process, the method proposed in this article can also be applied in torque/current control system to suppress harmonics.

REFERENCES

- [1] S. Cai, J. L. Kirtley, and C. H. T. Lee, "Critical review of direct-drive electrical machine systems for electric and hybrid electric vehicles," *IEEE Trans. Energy Convers.*, vol. 37, no. 4, pp. 2657–2668, Dec. 2022.
- [2] Y. Zhao, D. Li, X. Ren, and R. Qu, "Investigation of permanent magnet vernier machines from armature field perspective," *IEEE Trans. Emerg. Sel. Topics Power Electron.*, vol. 10, no. 3, pp. 2934–2945, Jun. 2022.
- [3] J. Ou, Y. Liu, R. Qu, and M. Doppelbauer, "Experimental and theoretical research on cogging torque of PM synchronous motors considering manufacturing tolerances," *IEEE Trans. Ind. Electron.*, vol. 65, no. 5, pp. 3772–3783, May 2018.
- [4] M. Hu, W. Hua, Z. Wang, S. Li, P. Wang, and Y. Wang, "Selective periodic disturbance elimination using extended harmonic state observer for smooth speed control in PMSM drives," *IEEE Trans. Power Electron.*, vol. 37, no. 11, pp. 13288–13298, Nov. 2022.
- [5] T. M. Jahns and W. L. Soong, "Pulsating torque minimization techniques for permanent magnet ac motor drives—A review," *IEEE Trans. Ind. Electron.*, vol. 43, no. 2, pp. 321–330, Apr. 1996.
- [6] Y. Cui, F. Zhang, L. Huang, and Z. Chen, "Analysis and verification of a cogging torque reduction method for variable flux memory permanent magnet machine," *Electronics*, vol. 10, no. 16, Aug. 2021, Art. no. 1913.
- [7] T. Husain, I. Hasan, Y. Sozer, I. Husain, and E. Muljadi, "Cogging torque minimization in transverse flux machines," *IEEE Trans. Ind. Appl.*, vol. 55, no. 1, pp. 385–397, Jan./Feb. 2019.
- [8] Y. Yang, N. Bianchi, G. Bramerdorfer, C. Zhang, and S. Zhang, "Methods to improve the cogging torque robustness under manufacturing tolerances for the permanent magnet synchronous machine," *IEEE Trans. Energy Convers.*, vol. 36, no. 3, pp. 2152–2162, Sep. 2021.
- [9] N. Nakao and K. Akatsu, "Suppressing pulsating torques: Torque ripple control for synchronous motors," *IEEE Ind. Appl. Mag.*, vol. 20, no. 6, pp. 33–44, Nov./Dec. 2014.
- [10] D. N. Zmood and D. G. Holmes, "Stationary frame current regulation of PWM inverters with zero steady-state error," *IEEE Trans. Power Electron.*, vol. 18, no. 3, pp. 814–822, May 2003.
- [11] T. M. Rowan and R. J. Kerkman, "A new synchronous current regulator and an analysis of current-regulated PWM inverters," *IEEE Trans. Ind. Appl.*, vol. IA-22, no. 4, pp. 678–690, Jul. 1986.
- [12] C. Xia, B. Ji, and Y. Yan, "Smooth speed control for low-speed high-torque permanent-magnet synchronous motor using proportional-integral-resonant controller," *IEEE Trans. Ind. Electron.*, vol. 62, no. 4, pp. 2123–2134, Apr. 2015.
- [13] X. Yuan, W. Merk, H. Stemmler, and J. Allmeling, "Stationary-frame generalized integrators for current control of active power filters with zero steady-state error for current harmonics of concern under unbalanced and distorted operating conditions," *IEEE Trans. Ind. Appl.*, vol. 38, no. 2, pp. 523–532, Mar./Apr. 2002.
- [14] L. Mirkin, "On dead-time compensation in repetitive control," *IEEE Control Syst. Lett.*, vol. 4, no. 4, pp. 791–796, Oct. 2020.
- [15] Y. Zuo, J. Zhu, X. Yuan, and C. H. Lee, "Two-degree-of-freedom quasi-pi controller for smooth speed control of permanent magnet vernier machine," in *Proc. IEEE Energy Convers. Congr. Expo.*, 2021, pp. 5022–5028.

- [16] M. Hu, W. Hua, G. Ma, S. Xu, and W. Zeng, "Improved current dynamics of proportional-integral-resonant controller for a dual three-phase FSPM machine," *IEEE Trans. Ind. Electron.*, vol. 68, no. 12, pp. 11719–11730, Dec. 2021.
- [17] Z. Gao, "On the centrality of disturbance rejection in automatic control," *ISA Trans.*, vol. 53, no. 4, pp. 850–857, Jul. 2014.
- [18] Y. Zuo, X. Zhu, L. Quan, C. Zhang, Y. Du, and Z. Xiang, "Active disturbance rejection controller for speed control of electrical drives using phase-locking loop observer," *IEEE Trans. Ind. Electron.*, vol. 66, no. 3, pp. 1748–1759, Mar. 2019.
- [19] Y. Zuo, J. Chen, X. Zhu, and C. H. Lee, "Different active disturbance rejection controllers based on the same order GPI observer," *IEEE Trans. Ind. Electron.*, vol. 69, no. 11, pp. 10969–10983, Nov. 2022.
- [20] Z. Song, Y. Wang, and T. Shi, "A dual-loop predictive control structure for permanent magnet synchronous machines with enhanced attenuation of periodic disturbances," *IEEE Trans. Power Electron.*, vol. 35, no. 1, pp. 760–774, Jan. 2020.
- [21] W.-H. Chen, "Disturbance observer based control for nonlinear systems," *IEEE/ASME Trans. Mechatron.*, vol. 9, no. 4, pp. 706–710, Dec. 2004.
- [22] B. Guo, S. Bacha, M. Alamir, A. Hably, and C. Boudinet, "Generalized integrator-extended state observer with applications to grid-connected converters in the presence of disturbances," *IEEE Trans. Control Syst. Technol.*, vol. 29, no. 2, pp. 744–755, Mar. 2021.
- [23] X. Yang, H. Hu, H. Hu, Y. Liu, and Z. He, "A quasi-resonant extended state observer-based predictive current control strategy for three-phase PWM rectifier," *IEEE Trans. Ind. Electron.*, vol. 69, no. 12, pp. 13910–13917, Dec. 2022.
- [24] B. Zhang, Y. Zuo, L. Quan, and X. Zhu, "Deadbeat active disturbance rejection controller for the current control of electric drives in the presence of two-step delay," in *Proc. IEEE 5th Int. Elect. Energy Conf.*, 2022, pp. 1924–1928.
- [25] G. Scelba, G. De Donato, A. A. Elsman, L. D. Tornello, G. Scarella, and F. G. Capponi, "Resolution of rotor position measurement: Modelling and impact on speed estimation," *IEEE Trans. Emerg. Sel. Topics Power Electron.*, vol. 10, no. 2, pp. 1992–2004, Apr. 2022.
- [26] T. Wang, Z.-Q. Zhu, N. M. A. Freire, Z. Wu, M. Foster, and D. A. Stone, "Study on noise and disturbance issues of generalized predictive speed control for permanent magnet synchronous machines," *IET Renew. Power Gener.*, vol. 15, no. 1, pp. 63–78, 2021.
- [27] Y. Zuo, J. Mei, C. Jiang, and C. H. Lee, "Digital implementation of deadbeat-direct torque and flux control for permanent magnet synchronous machines in the M-T reference frame," *IEEE Trans. Power Electron.*, vol. 36, no. 4, pp. 4610–4621, Apr. 2021.
- [28] J. Zhu, Y. Zuo, H. Chen, J. Chen, and C. H. Lee, "Deep-investigated analytical modeling of a surface permanent magnet vernier motor," *IEEE Trans. Ind. Electron.*, vol. 69, no. 12, pp. 12336–12347, Dec. 2022.



Yuefei Zuo (Member, IEEE) received his B.Eng. degree in electrical engineering and automation and his Ph.D. degree in power electronics and electrical drives both from Nanjing University of Aeronautics and Astronautics, Nanjing, China, in 2010 and 2016, respectively. From 2016 to 2019, he was a Lecturer with the School of Electrical and Information Engineering, Jiangsu University, Zhenjiang, China. He is currently a Senior Research Fellow with the School of Electrical and Electronic Engineering, Nanyang Technological University, Singapore. His research interests include power electronics, electric machines and drives, and advanced control strategies.



Jingwei Zhu received the B.Sc. degree in electrical engineering and automation from Zhejiang University, Hangzhou, China, in 2015 and the M.Phil. degree in electrical engineering from The Hong Kong Polytechnic University, Hong Kong, in 2018. Since August 2020, he has been working toward the Ph.D. degree in electrical and electronic engineering with Nanyang Technological University, Singapore.

He was the Edward R. Felber Power Fellowship Scholar with the University of Wisconsin-Madison, Madison, WI, USA, from 2018 to 2019 where he was with the Wisconsin Electric Machines and Power Electronics Consortium (WEMPEC), Madison, WI, USA. From September 2019 to July 2020, he was a Research Associate with the Center for System Intelligence and Efficiency (CSIE), Nanyang Technological University. His research interests include motor design and optimization, power electronics, bearingless motors, and direct-drive techniques.

Mr. Zhu was the recipient of the 2018 Edward R. Felber Power Fellowship awarded by University of Wisconsin-Madison.



Wenhao Jiang received the B.Sc. degree in electrical engineering and automation from the Yancheng Institute of Technology, Yancheng, China, in 2016. He is currently working toward the M.S. degree in electrical engineering with the School of Electrical and Information Engineering, Jiangsu University, Zhenjiang, China.

His research interests include power electronics, electric machines and drives, and advanced control strategies.



Shuangchun Xie (Student Member, IEEE) received the B.Sc. degree in electrical engineering and automation from the Nanjing University of Aeronautics and Astronautics, Nanjing, China, in 2017. He is currently working toward the Ph.D. degree in electrical and electronic engineering with the School of Electrical and Electronic Engineering, Nanyang Technological University, Singapore.

His research interests include power electronics, electrical machines and drives, and electric vehicle technologies.



Xiaoyong Zhu (Member, IEEE) received the B.Sc. and M.Sc. degrees in electrical engineering from Jiangsu University, Zhenjiang, China, in 1997 and 2002, respectively, and the Ph.D. degree in electrical engineering from Southeast University, Nanjing, China, in 2008.

During the period of doctoral study, his subject is electrical engineering, which mainly focuses on the design, analysis, and control of the type of hybrid-excited permanent magnet machine. Since 1999, he has been with Jiangsu University, where he is currently a Professor with the School of Electrical Information Engineering. In 2007–2008, he was a Research Assistant with the Department of Electrical and Electronic Engineering, University of Hong Kong, Hong Kong. From 2012 to 2013, he was a Visiting Professor with the Department of Energy-Funded Graduate Automotive Technology Education Center for Electric Drive Transportation, University of Michigan, Dearborn, MI, USA. In these areas, he has authored and coauthored more than 70 referred technical papers, and holds four patents. His current research interests include design and drive control of electric machines with wide-speed range, less rare-earth permanent magnet motor, and multipole permanent magnet motor.



Wen-Hua Chen (Fellow, IEEE) received the M.Sc. and Ph.D. degrees in automatic control from Northeastern University, Shenyang, China, in 1989 and 1991, respectively.

From 1991 to 1996, he was a Lecturer with the Department of Automatic Control, Nanjing University of Aeronautics and Astronautics, Nanjing, China. He held a research position and then a lectureship in control engineering with the Centre for Systems and Control, University of Glasgow, Glasgow, U.K., from 1997 to 2000. He is currently a Professor in Autonomous Vehicles with the Department of Aeronautical and Automotive Engineering, Loughborough University, Loughborough, U.K. He has authored or coauthored three books and 250 papers in journals and conferences. His research interests include the development of advanced control strategies and their applications in aerospace engineering, particularly in unmanned aircraft systems.

Dr. Chen is a Fellow of the Institution of Engineering and Technology and the Institution of Mechanical Engineers. He was a recipient of the EPSRC Established Career Fellowship Award.



Christopher H. T. Lee (Senior Member, IEEE) received the B.Eng. (First Class Honours) and Ph.D. degrees both in electrical engineering from the Department of Electrical and Electronic Engineering, The University of Hong Kong, Hong Kong, in 2009 and 2016, respectively.

He is currently an Assistant Professor with Nanyang Technological University, Singapore, and an Honorary Assistant Professor with The University of Hong Kong, Hong Kong. He was a Postdoctoral Fellow and then a Visiting Assistant Professor with the Massachusetts Institute of Technology, Cambridge, MA, USA. He is a Chartered Engineer in Hong Kong. In these areas, he has authored or coauthored one book, three books chapters, and more than 100 referred papers. His research interests include electric machines and drives, renewable energies, and electromechanical propulsion technologies.

Dr. Lee was the recipient of many awards, including NRF Fellowship, Nanyang Assistant Professorship, Li Ka Shing Prize (the best Ph.D. thesis prize), and Croucher Foundation Fellowship. He is currently an Associate Editor for IEEE TRANSACTIONS ON INDUSTRIAL ELECTRONICS, IEEE TRANSACTIONS ON ENERGY CONVERSION, IEEE ACCESS, and *IET Renewable Power Generation*.